Volume 3
Number 5
May 2024
Pages 919–1134

Energy Advances

rsc.li/energy-advances

ISSN 2753-1457

ROYAL SOCIETY OF CHEMISTRY

PAPER

Ejaz Hussain *et al.*

Promoting water-splitting reaction on TiO_2/gCN with Pd/SrO cocatalysts: H_2 evolution in the absence of a sacrificial reagent

Energy Advances

ROYAL SOCIETY OF CHEMISTRY

PAPER

View Article Online
View Journal | View Issue

Cite this: *Energy Adv.*, 2024, 3, 983

Promoting water-splitting reaction on TiO_2/gCN with Pd/SrO cocatalysts: H_2 evolution in the absence of a sacrificial reagent†

Khezina Rafiq,[a] Kashaf Ul Sahar,[a] Muhammad Zeeshan Abid,[a] Saira Attique,[a] Ubaid ur Rehman,[b] Abdul Rauf[a] and Ejaz Hussain *[a]

Depleting fossil fuel reserves and increased global warming have compelled researchers to seek a sustainable energy source. The current work presents an eco-friendly water splitting reaction on Pd–SrO@TiO_2/gCN photocatalysts. The catalysts reported herein have been synthesized using hydrothermal treatment, whereas cocatalyst (*i.e.* Pd/SrO) integration on graphitic carbon nitride (gCN) and rutile TiO_2 have been successfully completed *via* chemical reduction. The morphology and optical properties of the catalysts have been analyzed using XRD, Raman, FTIR, UV-Vis/DRS, PL, and SEM/EDX. The chemical composition, surface properties, electrochemical behaviour, and particle sizes were examined by XPS, EIS, AFM and BET technique followed by hydrogen evolution experiments. Evaluation of the sunlight-driven hydrogen generation activity of TiO_2, gCN, TiO_2/gCN, SrO@TiO_2/gCN, Pd@TiO_2/gCN, and Pd–SrO@TiO_2/gCN photocatalysts has been conducted and justified. The results reveal that the influence of TiO_2/gCN staggered band alignment, Schottky effect by palladium, metal/semiconductor interface engineering and elevation of Fermi energy level by the strontium oxide have efficiently enhanced the photocatalytic H_2 generation under sunlight. This study demonstrated no use of additional sacrificial reagents to prevent the back reactions and toxic side products where SrO reformed itself after consuming the holes during photoreaction. The combination of Pd and SrO was accountable for the maximum charge separation and relatively higher H_2 evolution on Pd–SrO@TiO_2/gCN catalysts that delivers 24.5 mmol g^{-1} h^{-1} of hydrogen. It is inferred that the aforementioned approach has potential to replace the conventional and costly catalysts used in hydrogen generation technologies.

Received 24th January 2024,
Accepted 1st April 2024

DOI: 10.1039/d4ya00045e

rsc.li/energy-advances

Introduction

The current state of affairs is witnessing a more severe global energy crisis and calamitous ecological events due to an increase in usage of fossil fuels.[1] In order to address these issues of energy scarcity and ecological and environmental protection, researchers have concentrated on sunlight-driven hydrogen production.[2,3] Various techniques like steam and autothermal reforming, H_2O/photochemical electrolysis, partial oxidation and Bosch process have been utilized for hydrogen production, but their main disadvantage is the high electricity consumption.[4–6] Hydrogen production through solar water splitting has the potential to accomplish the demanding energy goals. The utilization of solar energy for this purpose could be a viable, ecofriendly and sustainable approach that can mitigate CO_2 emissions.[7] Besides sunlight, water is a plentiful element found on earth.[8] Researchers are striving to fabricate reliable photocatalysts to achieve optimal H_2 production from solar water-splitting reactions.[9] Water splitting is an energetically uphill reaction that requires 237 kJ mol^{-1} energy for complete conversion of H_2O into O_2 and H_2.[10] There are significant challenges in the course of developing photocatalysts for water splitting, including difficulties arising from charge recombination and limited solar sensitivity in the visible light spectrum.[11] Effective fuel production (H_2) through water splitting could be achieved by fabricating advanced heterostructures.[12] The fusion of distinct quantum materials to create efficient heterostructures is drawing attention in the generation of maximum amounts of H_2 from photocatalytic water-splitting reactions.[13] Recently, different heterostructures have been introduced for water splitting, *e.g.*, GaTe/ZnI_2,[14] PG/GeP_2 and PG/SiP_2,[15] ZnO/ZnS,[16] $BiVO_4$/$Zn_3V_2O_8$,[17] NiS/NiS_2,[18] 2D-porous Co–Mo nitrides,[19] $BiVO_4$/CoFe MOF,[20] SnO_2@MoS_2,[21]

[a] *Institute of Chemistry, Inorganic Materials Laboratory 52S, The Islamia University of Bahawalpur, 63100, Pakistan. E-mail: ejaz.hussain@iub.edu.pk*
[b] *School of Physics, State Key Laboratory of Crystal Materials, Shandong University, Jinan 250100, Shandong, China*

† Electronic supplementary information (ESI) available. See DOI: https://doi.org/10.1039/d4ya00045e

C_2N/ZnSe,[22] Ru@RuO_2,[23] covalent triazine framework,[24] CdS/quantum dots,[25,26] MXene supported catalysts,[27] transition metal chalcogenides,[28] nanosphere heterostructures,[29] *etc.* Despite some benefits, there have been reports of several drawbacks associated with them, such as wide band gap, inadequate stability, toxicity and high price.[30] TiO_2 is a highly efficient photocatalyst that is commonly used due to its affordability, suitable electrical/optical properties, durability and hydrophilic nature.[31,32] Due to its high energy bandgap, the activation of TiO_2 is limited to the UV region, which represents only 4% of sunlight. Several methodologies have been developed to address this challenge, *e.g.*, metal oxide coating,[33] manufacturing of core–shell microspheres,[34] neutral network construction,[35] layering visible spectrum active photosensitizers,[36] and fabrication of heterostructures.[37] The loading/doping of metallic and non-metallic elements increases the charge separation and enhances the hydrogen production efficiency of photocatalysts by generating active sites.[38] Graphitic carbon nitride (gCN) is a 2D metal-free polymeric material[39] consisting of tris-triazine-based patterns (sp^2 hybridized, C/N = 3/4) with a sophisticated band gap (E_g = 2.67 eV).[40–42] Its remarkable conductivity, abundance of active sites, efficient physicochemical properties, thermal stability ($\sim$650 °C), and dielectric strength have garnered significant attention.[43–45] However, gCN possesses certain inherent limitations such as inadequate dispersibility and limited performance in sunlight.[46] To mitigate these issues, a composite/heterojunction can be fabricated by combining titania with gCN (TiO_2/gCN, type-II heterojunction) to restructure the stable photocatalysts. This type-II heterojunction facilitates the transfer of photogenerated charges over a long distance within the catalyst.[47] Furthermore, to improve the effectiveness of the TiO_2/gCN composite system, transition metals such as Pd, Pt, Cu, Ag and Au are often used to increase the electron concentration toward the active sites.[48,49] Palladium enables efficient carrier transport through the interface *via* Schottky junction due to its excellent electron-quenching ability.[50]

In the present study, Pd/SrO@TiO_2/gCN photocatalysts were synthesized through chemical reduction/hydrothermal reaction.[51] Pd and SrO nanoparticles were *in situ* deposited on the surfaces of the composite (TiO_2/gCN). The inclusion of SrO elevated the Fermi energy level of the semiconductor during photoreaction and enhanced the electron transport toward palladium active sites.[52,53] The utilization of SrO (metal oxide) eliminated the need for supplementary sacrificial reagents by consuming holes. The current study found that SrO had a dual effect in increasing the rate of hydrogen evolution by originating OH^- ions during the photoreaction that consumes holes (h^+) and increasing the Fermi level. The optical absorption, structural and chemical composition and precise surface area of the as-synthesized photocatalysts were rigorously characterized. The multifaceted nanoscale Pd–SrO@TiO_2/gCN photocatalysts were identified as a promising and innovative solution for global energy crises and environmental issues by serving as an efficient promoter of hydrogen production.

Experimental

The required chemicals, synthesis of the photocatalysts (gCN, TiO_2/gCN, and Pd@TiO_2/gCN) and instruments utilized for characterization are discussed in Section S1 of the ESI.†

Synthesis of Pd–SrO@TiO_2/gCN

The conventional procedure involved the dispersion of gCN in deionized water and stirring for 2 h at 25 °C, followed by 10 minutes of sonication. TiO_2 was then added, and further sonication was carried out for 8–10 minutes. A 2% solution of palladium(II) acetate (2 mL) was introduced into the slurry and stirred for 30 minutes. Strontium chloride solution was added dropwise after stirring to achieve the desired metal loading. The mixture was sonicated for 5 minutes, then reduced with $NaBH_4$, and 20 mL of DI-H_2O was added. Then, hydrothermal treatment was conducted by placing it in an oven at 150 °C for 2 hours. The slurry was removed from the autoclave and filtered. The synthesis scheme of the Pd–SrO@TiO_2/gCN photocatalysts is depicted in Fig. S1 (ESI†).

Hydrogen production experiment

The hydrogen evolution experiments were conducted in a 140-mL quartz reactor using sunlight for photoreactions. As shown in Table S5 (ESI†) and Fig. 7(b), 5 mg of photocatalysts (as synthesized) were introduced into the reactor with 25 mL of deionized water. Before the photocatalytic reaction, the reactor's contents were subjected to purging using highly pure N_2, which served as a carrier gas to eliminate oxygen present in the reactor. The measured photon flux was $\sim$6.5 mW cm^{-1} during the photoreaction, using the following eqn (1):

$$\phi = \frac{\text{Number of photons}}{\text{area} - \text{second}} \quad (1)$$

Hydrogen production analysis was carried out by extracting the reactor's head space gas at various time intervals. This was done by injecting 0.5 mL of the sample into the GC sample holder, which was equipped with a thermal conductivity detector (TCD) and capillary molecular sieve. Hydrogen evolution was measured using an internal standard calibration curve. The experiments were conducted in the month of October 2023, under clear sky conditions in South Punjab, Pakistan, at a latitude of 29° 23′ 44.5956″ N and a longitude of 71° 41′ 0.0024″ E. Each sample was tested at least three times. The hydrogen evolution rates were calculated by using units of mmol g^{-1} (Fig. 5(a) and (b)) and mmol g^{-1} h^{-1} (Fig. 5(c)), while analyzing the photocatalytic activities under optimized conditions (Section S2 of the ESI†). The quantum yield of each synthesized photocatalyst was individually computed, ensuring accuracy in analysis by using eqn (2):

$$\text{Quantum efficiency} = 2 \times \frac{N(H_2)}{N(\text{photons})} \times 100 \quad (2)$$

The maximum observed quantum efficiency of Pd–SrO@TiO_2/gCN was 18.5%. A comparison of A. Q. E. with previous literature is presented in Table S8 (Section S3 of the ESI†).

Result and discussion

Crystallinity/structural assessment

The photocatalysts' crystallization and phase purity were assessed through X-ray diffraction (XRD) analysis within the range of 20°–80° 2θ. XRD offered significant insights into the atomic and molecular composition of the as-synthesized material. The XRD spectra of all as-synthesized photocatalysts are represented in Fig. 1(a) and (b). When examining the XRD pattern of gCN, distinct diffraction peaks (according to JCPDS number 87-1526) that aligned with its crystal structure were noticed. The (002) plane in the crystal structure is represented by a prominent peak typically found between 13° and 28° 2θ; its position depended upon the sample preparation and synthesis conditions.[54] This pattern determined the interlayer spacing within the gCN layer. A broad peak ranging from 25° to 30° 2θ was observed, and it was associated with the amorphous/distorted area in the gCN structure, corresponding to different crystallographic planes. This intense peak represents the well-ordered and highly crystalline structure of the stacked conjugated aromatic system. It confirmed the presence of nitrogen-bridged repeated tris-triazine subunits, as depicted in Fig. 1(a).

The XRD peaks of tetragonal rutile-TiO_2 matched the JCPDS number 75-1748, as depicted in Fig. 1(b). The diffraction peaks of rutile-TiO_2 were located at 27.435° (110), 36.079° (101), 39.189° (110), 41.238° (200), 44.042° (111), 54.319° (210), 56.624° (211), 62.757° (220), 64.045° (002), 65.508° (310), 69.002° (221), 69.800° (112), 72.416° (311), 74.398° (320) and 76.536° (202), respectively. The observed peaks of TiO_2/gCN, related to both TiO_2 and gCN, are depicted in Fig. S2 (ESI†) in the range of 25°–30°, while in the Pd@TiO_2/gCN and Pd–SrO@TiO_2/gCN photocatalysts, the diffraction patterns of palladium have been located at 39.92° (111) and 45.53° (200), respectively.[55] In Pd–SrO@TiO_2/gCN, two minor patterns emerged within the range of 24°–29° 2θ, due to the existence of strontium oxide. The cocatalysts were highly reactive and vastly dispersed over the surface of TiO_2/gCN; thus they did not show any metallic characteristics.

The FTIR spectra of gCN and TiO_2 are presented in Fig. 1(c). In the gCN spectrum, the typical strong peaks were observed at 1113.15 and 1629.14 cm^{-1} indicating the presence of carbon

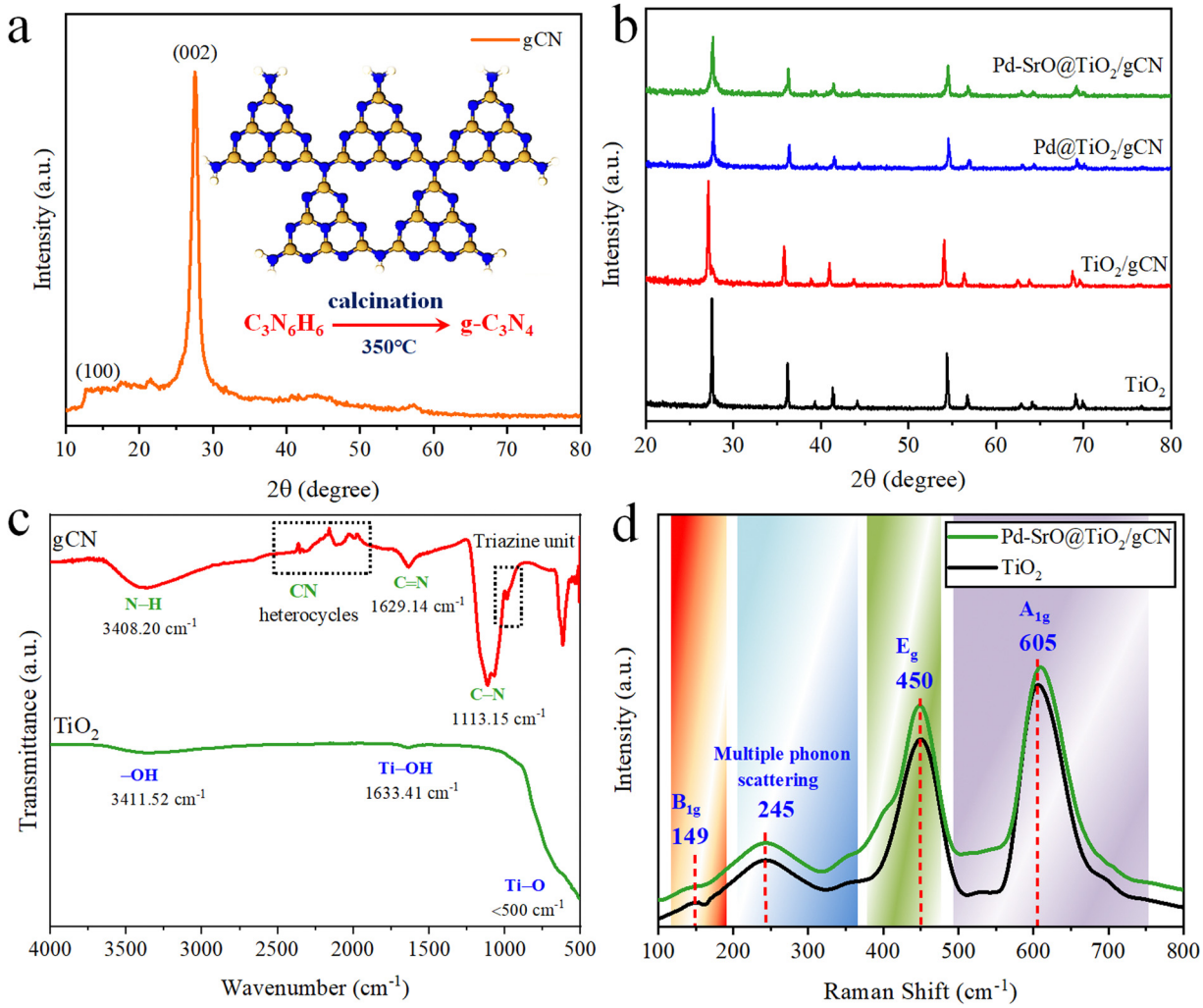

Fig. 1 (a) XRD pattern of gCN; (b) XRD patterns of TiO_2, TiO_2/gCN, Pd@TiO_2/gCN, and Pd–SrO@TiO_2/gCN; (c) FTIR patterns of TiO_2 and gCN; (d) Raman bands of TiO_2 and Pd–SrO@TiO_2/gCN.

and nitrogen (C–N stretching). A broad pattern at 3408.20 cm^{-1} indicates N–H bending vibration, confirming the presence of amino/amine group. A few minute peaks of C–H and C–C aromatic stretching were observed due to the presence of hydrocarbon impurities and structural functionalization.

The shoulder peak detected at 809 cm^{-1} confirmed the existence of tris-triazine subunits. In the case of TiO_2 lattice spectrum, a strong peak of Ti–O bond stretching vibration appeared at <500 cm^{-1}. The peaks related to O–H group have been located at 1633.41 and 3411.52 cm^{-1}. These peaks originated due to stretching or bending vibrations of O–H and Ti–O–H bonds. The confirmation of these peaks indicated the possibility of interfacial connection between gCN and TiO_2.

The electronic excitation, band gap analysis, structural transformations and vibrational properties were analyzed by Raman spectroscopy (non-destructive technique), as shown in Fig. 1(d). The Raman spectra of TiO_2 and Pd–SrO@TiO_2/gCN were investigated at λ = 632 nm (resonance enhancement; scan range 100–900 cm^{-1}). At this wavelength, the vibrational modes of the photocatalysts are more detectable. TiO_2 showed specific vibrational patterns, *i.e.*, the band at 149 cm^{-1} corresponding to B_{1g} mode, the band at 450 cm^{-1} corresponding to E_g mode, and the band at 605 cm^{-1} corresponding to A_{1g} mode. The band at 149 cm^{-1} typically represents the stretching in the Ti–O bond. The prominent band at 605 cm^{-1} (in Pd–SrO@TiO_2/gCN) depicts the existence of metal/metal-oxide cocatalysts and nitrogen bridged tris-triazine subunits. The catalysts, TiO_2 and Pd–SrO@TiO_2/gCN, were found to have similar patterns, confirming their purity. A discrete wide band at 245 cm^{-1} is due to multiple phonon scattering, where the particle interacted with multiple phonons during its journey through the photocatalyst. In the current work, XRD and Raman investigations have been effectively correlated, depicting Pd–SrO@TiO_2/gCN as a well-organized crystalline photocatalyst.

Optical studies and electronic property analyses

The electronic properties, concentration, and compound identity were analyzed using UV-DRS spectroscopy. The UV-DRS spectrum of Pd–SrO@TiO_2/gCN is illustrated in Fig. 2(a). TiO_2

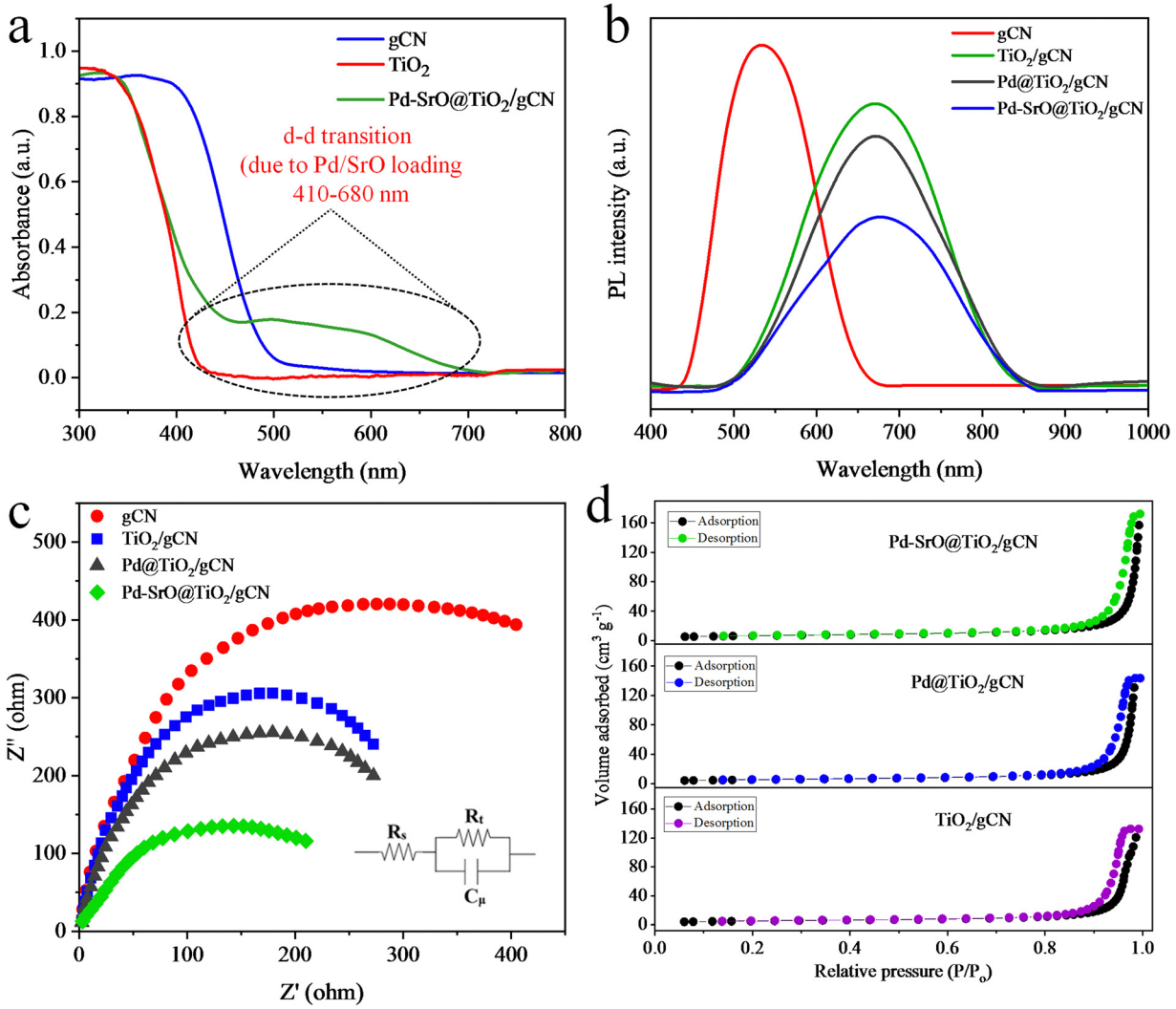

Fig. 2 (a) UV-DRS spectra of TiO_2, gCN and Pd–SrO@TiO_2/gCN; (b) PL spectra at the excitation wavelength of 325 nm; (c) EIS results of gCN, TiO_2/gCN, Pd@TiO_2/gCN, and Pd–SrO@TiO_2/gCN; (d) BET analyses of TiO_2/gCN, Pd@TiO_2/gCN and Pd–SrO@TiO_2/gCN.

exhibits a spectral response in the UV region, while gCN exhibited spectral response in the visible region. The semiconductor (TiO_2/gCN) loaded with Pd/SrO showed an absorption edge at 457 nm and a wide peak of adsorption from 410–680 nm, as depicted in Fig. 2(a). The adsorption edges of TiO_2 and gCN were located at 430 nm and 500 nm, respectively. The Pd–SrO@TiO_2/gCN displayed an energy gap (E_g) at 2.97 eV, which is intermediate between the energy gaps (E_g) of TiO_2 (3.05 eV) and gCN (2.68 eV), as depicted in Fig. S3 (ESI†). Pd–SrO@TiO_2/gCN was discovered to be the most efficient photocatalyst in the series, as a result of the synchronization of heterojunction and addition of metal/metal oxide cocatalyst deposition. The Schottky effect by palladium, coupled with the hole consumption and promotion of electrons toward metal active sites by SrO, eventually reduced the rate of charge recombination and resulted in maximum H_2 evolution by Pd–SrO@TiO_2/gCN.

The electronic structure, charge carrier dynamics, and defect states in the synthesized materials were identified through photoluminescence spectroscopic investigation, as presented in Fig. 2(b). The peaks in the PL spectra potentially indicated the existence of defect-related emissions. These defects introduced the energy levels within the band gap that can trap charge carriers. The PL emission of gCN was in the range of 420–660 nm, whereas the incorporation of rutile TiO_2 shifts the emission to 500–850 nm, due to subsequent charge transfer between gCN and TiO_2. The intensity of recorded PL emission is directly proportional to the maximum charge recombination rate and the low photocatalytic efficiency of the material, while the low intensity of PL emission signifies low charge recombination rate and maximum photocatalytic efficiency of the material. It is well known that the PL emission by gCN locates at 512 nm, whereas the peak of TiO_2 originates at 812 nm. In this study, broad spectra were observed between 470 and 865 nm for TiO_2/gCN, Pd@TiO_2/gCN, and Pd–SrO@TiO_2/gCN. The wide band with the least intensity of emission was observed in the case of Pd–SrO@TiO_2/gCN, which resulted in maximum charge separation and the highest photocatalytic activity. The PL results are consistent with UV/DRS in light adsorption evaluation and band edge determination.

The electron impedance spectroscopic analyses of Pd–SrO@TiO_2/gCN, Pd@TiO_2/gCN, TiO_2/gCN and gCN provide insights on their surface properties, electrolytic interaction and electrochemical behaviour,[56] as indicated in Fig. 2(c). The sizes of the depressed semicircles have been associated with the magnitude of the charge transfer resistance of the corresponding electrodes. Pd–SrO@TiO_2/gCN has a smaller radius compared to TiO_2/gCN and Pd@TiO_2/gCN, indicating a lower electron transfer resistance that inhibits charge recombination.[57] It is proposed that the separation and transfer of photogenerated charges could be effectively promoted by combining a certain amount of SrO and Pd (1.8 : 0.2 wt%), thereby enhancing the effect of photocatalytic hydrogen production.

Morphological analysis

The morphology and structure of Pd–SrO@TiO_2/gCN have been effectively analyzed through SEM images, as depicted in Fig. 3(a) at 3.0 μm and Fig. 3(b) at 1.0 μm resolution. The SEM images revealed a rough surface with cracks, pores, and thick, blocky bulk material. These properties of Pd–SrO@TiO_2/gCN greatly influenced its hydrogen production activity. The numerous cracks and pores arose due to the deposition of cocatalysts over TiO_2/gCN heterostructures in Pd–SrO@TiO_2/gCN, as compared to the previously reported TiO_2,[58] gCN,[59] and Pd@TiO_2/gCN[60] surfaces. These micro-cracks have increased the surface area of the material, enhanced the number of active sites, and increased the immobilization and agglomeration of metal nanoparticles, eventually resulting in vigorous photocatalytic activity. The rough surface enhanced the light absorption efficiency of Pd–SrO@TiO_2/gCN. The small height differences on the rough surface suggested the existence of nanoparticles that effected the overall photocatalytic efficiency and the optical and electronic properties of Pd–SrO@TiO_2/gCN.

The determination of elemental composition, identification of impurities, and quantitative analysis were conducted using electron-dispersive X-ray spectroscopy.[61] The confirmation of the presence of dual cocatalysts (Pd/SrO) on the surfaces of the Pd–SrO@TiO_2/gCN was provided by EDX. The purity of photocatalysts was confirmed through EDX analysis, which established the existence of C, Sr, N, Ti, O, and Pd, as shown in Fig. 3(c).

AFM revealed the topological structure of Pd–SrO@TiO_2/gCN as shown in ESI,† Section S1 and Fig. S4(a)–(e). These 2D and 3D images, in light and dark, demonstrated the well-organized homogenous patterns of Pd–SrO@TiO_2/gCN and the immobilization of TiO_2 and Pd–SrO contents within the layers. The particle distribution of Pd–SrO@TiO_2/gCN covers a range of 5 × 5 μm. The 2D and 3D AFM images were taken under light irradiation by a photoinduced effect; the high region (warmer region) is shown at 3.5–3.25 μm in red, while the lower region appeared at the range of 0.7–0.25 μm in blue. The maximum adhesion force and variations in photocatalyst composition were observed, as shown in Fig. S3(c) (ESI†). The microscale hills and roughness pattern of Pd–SrO@TiO_2/gCN were observed in the 3D image under light irradiation, as depicted in Fig. S4(a) (ESI†). The particle size ranged from 0.353–3.53 μm, according to the size distribution pattern of the histogram in Fig. S4(e) (ESI†). A regular roughness of 1 μm was measured. AFM was also conducted in the absence of external light sources to obtain the baseline images of the material's inherent properties, and structural defects could be clearly observed in (Fig. S4(b) and (d) (ESI†); 3D and 2D images). The AFM results are in good agreement with SEM, as shown in Fig. 3(a) and (b).

Surface analysis

BET analysis characterized the surface area and porosity of Pd–SrO@TiO_2/gCN, Pd@TiO_2/gCN and TiO_2/gCN as well as their potential to harness sunlight.[48] Certain pore structures can enhance the reactant diffusion and accessibility to active sites. TiO_2/gCN showed low nitrogen adsorption, indicating a low number of active sites compared to Pd@TiO_2/gCN and Pd–SrO@TiO_2/gCN. The inclusion of Pd on TiO_2/gCN resulted in a

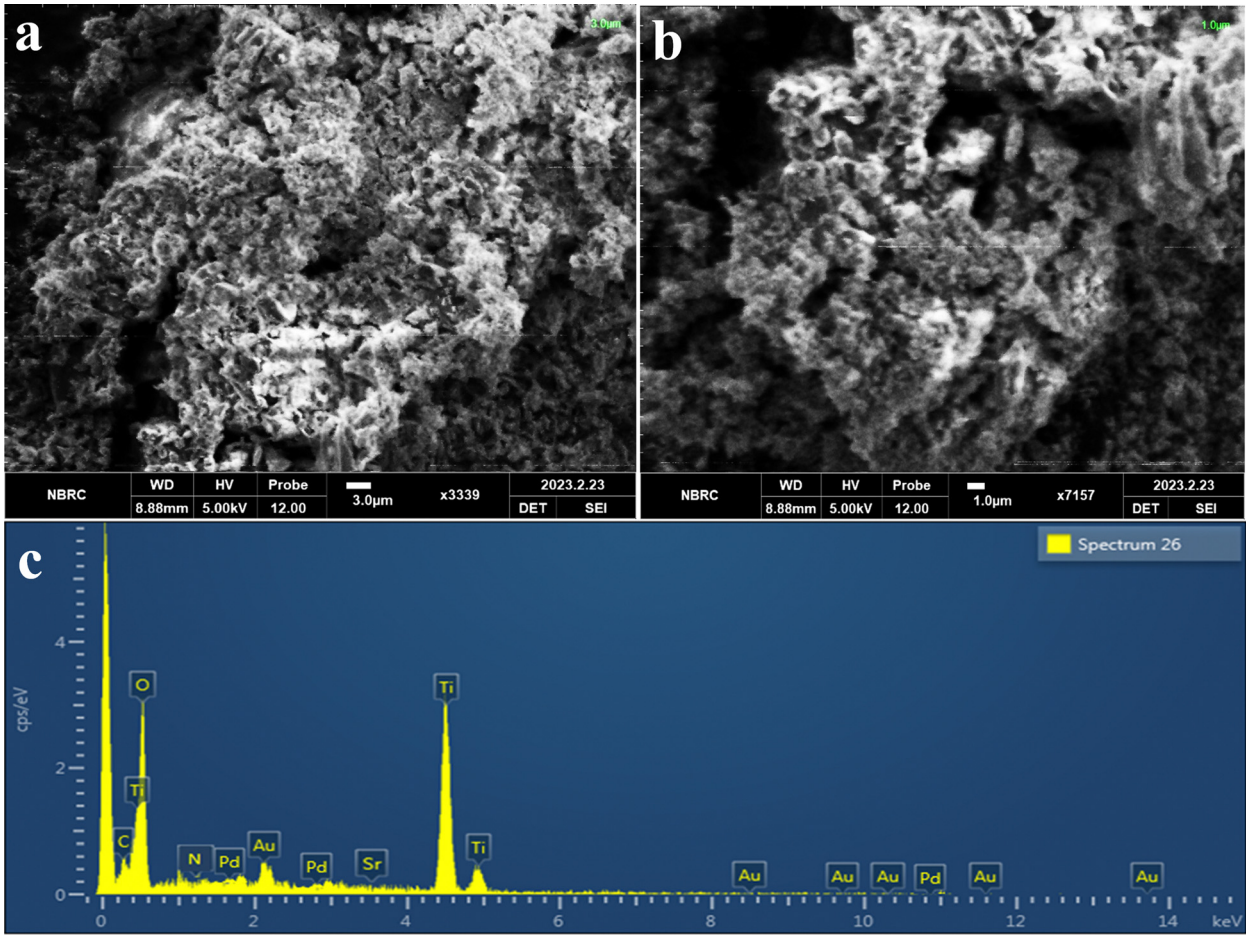

Fig. 3 SEM images of Pd–SrO@TiO_2/gCN at (a) 3.0 μm and (b) 1.0 μm; (c) EDX of Pd–SrO@TiO_2/gCN.

BET surface area of 29.2 m^2 g^{-1} for Pd@TiO_2/gCN. In the case of Pd–SrO@TiO_2/gCN, there was a significant increase in nitrogen adsorption capacity, leading to an increase in BET surface area to 32.8 m^2 g^{-1}. It has been observed that an appropriate amount of cocatalysts (Pd and SrO) promote good dispersion on TiO_2/gCN. Additionally, a high surface area contributed to the enhancement of photocatalytic hydrogen generation performance. Pd–SrO@TiO_2/gCN was found to be mesoporous, exhibiting a type II hysteresis loop where the material exhibits a steep absorption branch and a less steep desorption branch after N_2-adsorption/desorption investigations.[62] Moreover, the shape of the hysteresis loop and the volume adsorbed (as shown in Fig. 2(d)), indicating the occurrence of a high number of accessible active sites, ensured an all-out hydrogen evolution by Pd/SrO@g-C_3N_4/TiO_2.

Crystal structure and chemical composition analysis

The XPS survey of Pd–SrO@TiO_2/gCN detected Ti, O, N, C, Pd, and Sr, as shown in Fig. 4. TiO_2 exhibited two peaks, as depicted in Fig. 4(a). 457.81 eV represented Ti $2p_{2/3}$, while 464.4 eV represented Ti $2p_{1/2}$ energy level of the rutile phase of titanium.[63,64] The presence of O 1s originated from TiO_2 and SrO, at 529.04 eV (O^{2-}), 531.09 eV (non-lattice, –OH) and 534.13 eV (Sr–O), as depicted in Fig. 4(b). The non-lattice oxygen in the material referred to the presence of free oxygen on the surface of the material in different chemical states. The core level peak of C 1s was located at 285.02 eV, while the specific peak at 289 eV, as shown in Fig. 4(e), indicated the presence of N=C–C coordination. This coordination indicated nitrogen and carbon bonding in gCN, which confirmed the presence of gCN in the photocatalysts. The location of the energy level peak at 398.6 eV in the high-resolution N 1s spectrum indicated the specific chemical environment for the sample. This peak suggested the presence of the azo functional group (C=N–C). The pattern at 400 eV indicated the presence of the amino functional group (C–N–H) and tertiary nitrogen, as depicted in Fig. 4(f). The peak at 335.58 eV indicated the energy level of Pd $3d_{5/2}$ while the peak at 340.92 eV indicated the energy level of Pd ($3d_{3/2}$), confirming the existence of palladium metal nanoparticles having zero oxidation state, as presented in Fig. 4(c). The peak at 133.0 eV indicated the energy level of Sr $d_{5/2}$, while the peak at 135.0 eV showed the energy level of Sr $3d_{3/2}$, indicating the existence of strontium metal nanoparticles, as presented in Fig. 4(d). The highest photocatalytic activity of Pd–SrO@TiO_2/gCN attributed to palladium in pure metallic state and SrO; these findings are well-matched with the EDX results.

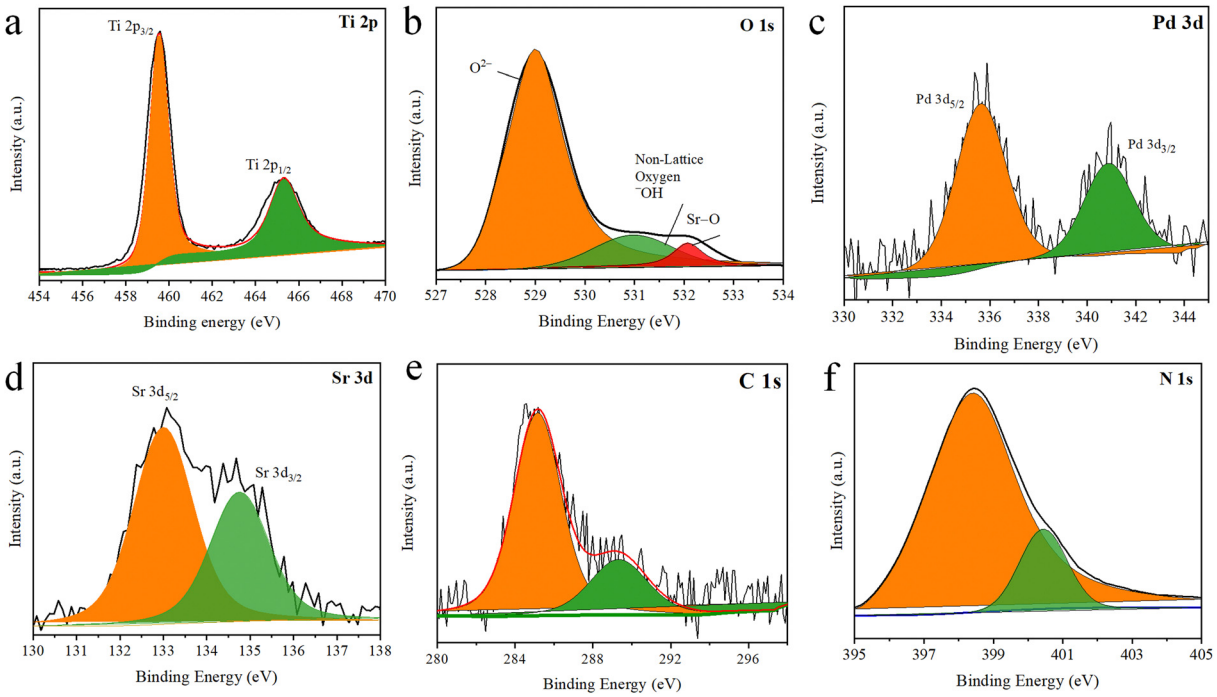

Fig. 4 Pd–SrO@TiO_2/gCN XPS spectra at the core level (a) Ti 2p, (b) O 1s, (c) Pd 3d, (d) Sr 3d, (e) C 1s (f) N 1s.

Hydrogen production activity

The hydrogen generation activity of each photocatalyst was evaluated by optimizing a 5 mg dose and subjecting them to photocatalytic reaction at pH 7.5, as shown in Table S3 (ESI†) and Fig. 7(d), under solar irradiation for 6 h, as shown in Table 1. In the absence of sunlight, no photocatalytic reaction is observed. The observed rate of H_2 evolution over rutile TiO_2 was 2.27 (mmol g^{-1}) and 0.462 (mmol g^{-1} h^{-1}). The gCN produced hydrogen at the rate of 12.42 (mmol g^{-1}) and 2.07 (mmol g^{-1} h^{-1}), which was high compared to TiO_2. The TiO_2/gCN composite produced H_2 at the rate of 32.4 (mmol g^{-1}) and 5.41 (mmol g^{-1} h^{-1}). The combination of TiO_2 and gCN in a heterojunction capitalizes on the individual strength and complementary characteristics of each material, leading to the synergistic effect that boosts the efficiency of hydrogen production. The SrO@TiO_2/gCN (SrO: 2 wt%) composite produced H_2 at the rate of 56.712 (mmol g^{-1}) and 9.452 (mmol g^{-1} h^{-1}). The Pd@TiO_2/gCN (Pd: 2 wt%) composite produced H_2 at the rate of 101.3 (mmol g^{-1}) and 16.9 (mmol g^{-1} h^{-1}). The presence of palladium enhanced the hydrogen production activity due to quenching of electrons from the conduction band of TiO_2.[65,66] This synergistic effect is due to the improved charge separation. The metal-coordinated electrons became available for reducing water into hydrogen gas. However, the observed rate of H_2 evolution over Pd–SrO@TiO_2/gCN (Pd : SrO = 1.8 : 0.2 wt%) was significantly higher than that of the other as-synthesized photocatalysts. The Pd–SrO@TiO_2/gCN composite produced H_2 at the rate of 147.04 (mmol g^{-1}) and 24.5 (mmol g^{-1} h^{-1}), which is actually a high amount of H_2 generated as compared to other synthesized photocatalysts as shown in Fig. 5(a)–(c). Fig. 5(a) depicts the rate of hydrogen evolution (mmol g^{-1} h^{-1}) by each as synthesized in 360 consecutive minutes under optimized conditions (Fig. 7(a)–(f)). Fig. 5(b) depicts the maximum rate of hydrogen evolution (mmol g^{-1}) by each as-synthesized photocatalyst (TiO_2, gCN, TiO_2/gCN, SrO@TiO_2/gCN, Pd@TiO_2/gCN, and Pd–SrO@TiO_2/gCN) over time (min^{-1}). Fig. 5(c) illustrates the comparative analysis of H_2 generation at the rate of (mmol g^{-1} h^{-1}) by each as-synthesized photocatalyst, showing how much hydrogen evolved during 1–6 h.

Table 1 Hydrogen generation activities at the rate of (mmol g^{-1})/(mmol g^{-1} h^{-1}) by as-synthesized photocatalysts

S. no.	Photocatalyst[a]	Metal loading (wt%)	H_2 production (mmol g^{-1})	H_2 production (mmol g^{-1} h^{-1})
1	Rutile-TiO_2	0	2.77	0.462
2	gCN	0	12.42	2.07
3	TiO_2/gCN	0	32.4	5.41
4	SrO@TiO_2/gCN	2	56.7	9.45
5	Pd@TiO_2/gCN	2	101.3	16.9
6	Pd–SrO@TiO_2/gCN	1.8 : 0.2	147.04	24.5

[a] 5 mg catalyst amount, photon flux = 6.5 mW cm^{-1}, reactor volume = 140 mL.

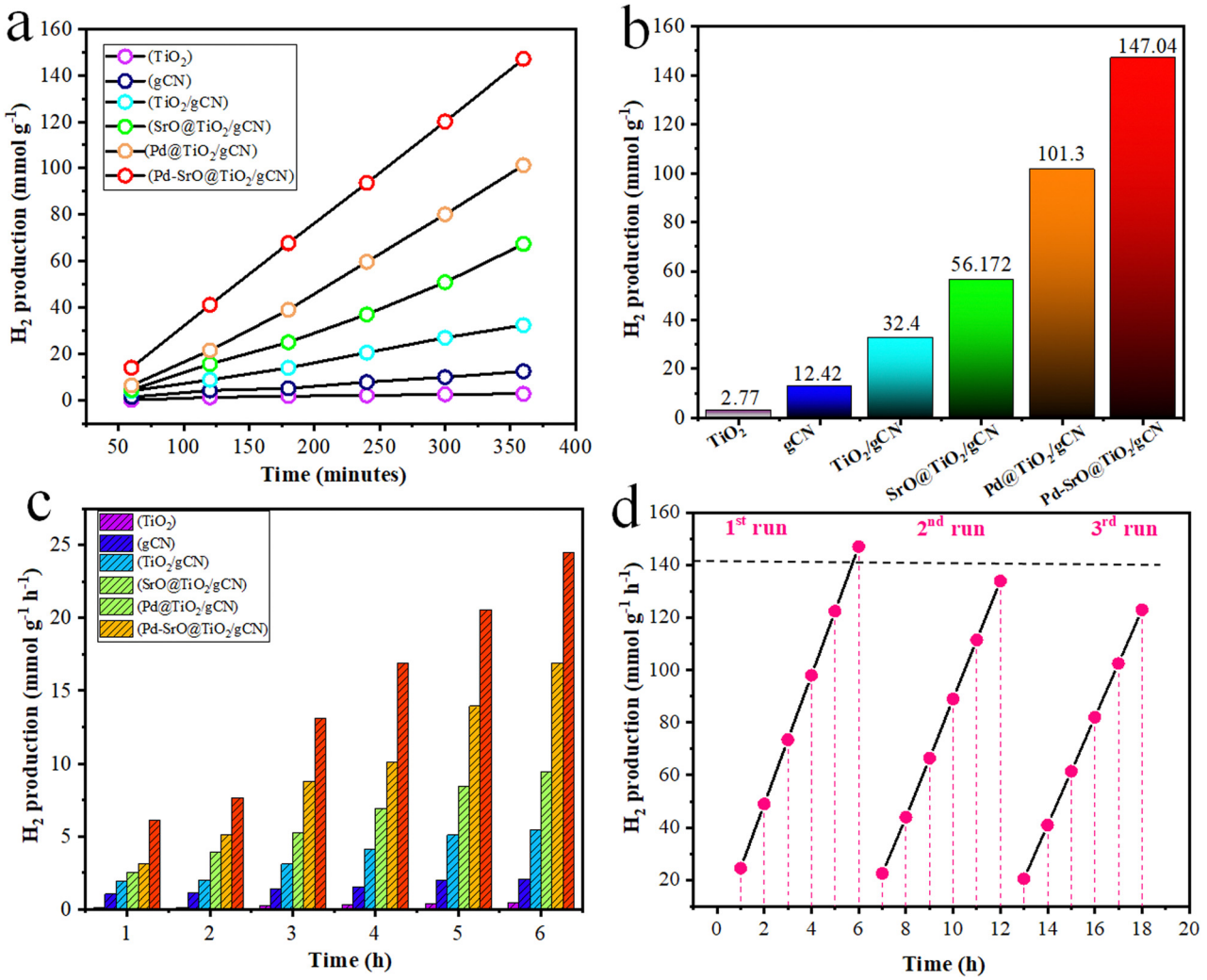

Fig. 5 Hydrogen generation activity results: (a) H_2 generation at the rate of (mmol g^{-1}), with (b) representing the total hydrogen production percentage by each photocatalyst; (c) H_2 generation at the rate of (mmol g^{-1} h^{-1}) by the as-synthesized photocatalysts; (d) a 3-run recyclability test of Pd–SrO@TiO_2/gCN.

Water splitting mechanism by Pd–SrO@TiO_2/gCN

The photocatalyst's band structure plays a crucial role in determining the suitability of its energy levels for the water splitting reaction, and it influences the progression of the reaction along the reaction coordinate. In order to achieve efficient water splitting, the semiconductor's valence band should have a higher energy level than the oxidation potential of water (O_2/H_2O), while the semiconductor's conduction band should have a lower energy level than the reduction potential of water (H^+/H_2). This allows energized electrons from the conduction band to participate in the reduction half reaction and convert protons into hydrogen.[67] In context to water splitting, two half reactions have taken place (eqn (3) and (4));

$$\text{Water oxidation reaction; } 2H_2O + 4h^+ \rightarrow O_2 + 4H^+ \quad (3)$$

$$\text{Water reduction reaction; } 4H^+ + 4e^- \rightarrow 2H_2 \quad (4)$$

To achieve the necessary ΔG° value, reactions need to proceed spontaneously, (see eqn (5)–(8)).[68,69]

$$\text{Photocatalyst} \rightarrow e^- + h^+ \quad (5)$$

$$2H_2O + 2e^- \rightarrow H_2 + 2OH^- \quad E^\circ = 0.0\ \text{V} \quad (6)$$

$$2OH^- + 2h^+ \rightarrow \frac{1}{2}O_2 + H_2O \quad E^\circ = 1.23\ \text{V} \quad (7)$$

$$H_2O \rightarrow H_2 + \frac{1}{2}O_2 \quad \Delta G = 237\ \text{kJ} \quad (8)$$

In the current work, the work function of palladium (5.55 eV) is greater than that of gCN (4.62 eV) and TiO_2 (4.2 eV). Due to the disparity in energy levels, the electrons within the conduction band (CB) of gCN possess adequate energy to transfer to the CB of TiO_2. Upon the adsorption of photons in the gCN region, the electron/hole pairs emerge. The electrons, which attain more energy due to the misaligned band structure, can proceed to transfer to the TiO_2 region, which typically exhibits a lower

energy conduction band. The holes in the valence band (VB) of TiO_2 start to flow toward the VB of gCN (typically, from lower → higher energy level). The presence of staggered band alignment at the heterojunction interface results in Schottky barrier formation, serving for effective charge separation. Meanwhile, the palladium metal exhibits a high work function, and the electrons originated in the CB of TiO_2 move in a continuous flow towards the metal active sites until the system reaches equilibrium, where they eventually participate in the H^+ ion reduction to generate the molecular hydrogen gas. UV-Vis absorption spectroscopy was utilized to gather information regarding the optical properties of gCN, TiO_2, and their composite. The formation of a staggered heterojunction within the photocatalytic system was indicated by changes in the absorption edge or bandgap energy.

The electronic structure of the as-synthesized photocatalysts and the gCN/TiO_2 interface within Pd–SrO@TiO_2/gCN was investigated using the XPS technique. The change in electronic structure due to heterojunction formation was indicated by shifts in the core levels and valence band positions. The intimate contact between gCN and TiO_2, as well as the presence of loaded cocatalysts, was confirmed by SEM. EDX provided elemental confirmation of gCN/TiO_2, verifying the distribution of C, N, Ti, O, Pd, and Sr elements and their spatial arrangement at the interface. By utilizing these experimental techniques, conclusive evidence has been provided to support the formation of a type II staggered heterojunction between gCN and TiO_2 in the composite photocatalyst system.

The presence of SrO functions as a sink for holes, ensuring that they don't prematurely combine with electrons in the semiconductor. Once the holes are transferred to the CB of the metal oxide, they become involved in the oxidation of water. At the interface among the semiconductor–metal oxide, the holes prefer to move to the metal oxide's CB, preventing them from combining with electrons in the semiconductor (see eqn (9) and (10)). The rate of recombination of charge carriers is reduced to the maximum level. SrO converts to $Sr(OH)_2$ after encountering H_2O molecules and generates OH^- ions; the OH^- ions eagerly consume holes from the semiconductor's valence band. When the level of OH^- ions is surpassed in the photoreactor, they eventually begin to react with water, resulting in the production of H^+ ions. These H^+ ions then react with previously generated H^+ ions over the palladium active sites, ultimately leading to highly effective hydrogen evolution.[70]

$$h_{VB} + H_2O \rightarrow OH^- + H^+ \quad (9)$$

$$h_{VB} + OH^- \rightarrow OH^* \quad (10)$$

The strontium oxide once again reconstitutes itself following the reaction, resulting in the creation of a byproduct that adheres to the surface of the TiO_2/gCN composite. This was confirmed through XPS, UV-Vis DRS, and H_2 evolution experiments. The utilization of SrO enhanced the rate of hydrogen

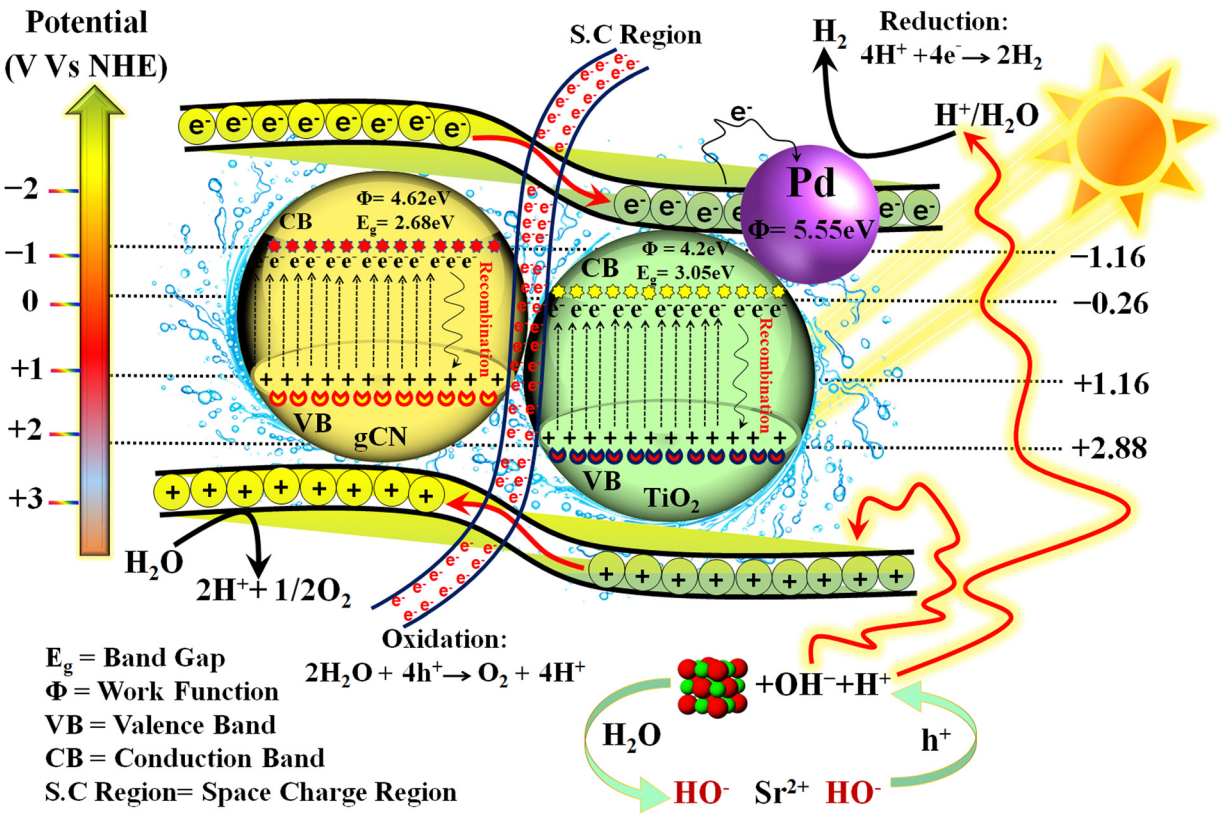

Fig. 6 The mechanism of H_2 evolution through solar water splitting using Pd–SrO@TiO_2/gCN.

production to the maximum level, while it eventually eliminated the need of any additional sacrificial reagents; the undesirable role of sacrificial reagents is presented in Table S4 (ESI†) and Fig. 7(c). Hence, the maximum reduction in activation energy threshold separating the oxidation from the reduction potential was achieved upon the introduction of the dual cocatalysts (strontium oxide and palladium) onto the semiconductor surfaces. Palladium nanoparticles that are spherical or quasi-spherical are frequently utilized in palladium non-traditional SPR effect under specific circumstances.[71] The interaction of palladium surface and photons occasioned in the generation of hot e^-/h^+. Subsequently, the advent of hot holes on palladium surfaces is a result of the transfer of hot electrons towards the semiconductor's CB. The plasmon is characterized by plasmon frequency (ω_p),[68] which is determined by following eqn (11);

$$\omega_p = \sqrt{\frac{ne^2}{\mathcal{E}^\circ m}} \tag{11}$$

The remarkable increase in hydrogen production was achieved through Pd–SrO@TiO_2/gCN (24.5 mmol g^{-1} h^{-1}), which efficiently suppressed the back-reaction. The mechanism of H_2 evolution through solar water splitting using Pd–SrO@TiO_2/gCN is shown in Fig. 6.

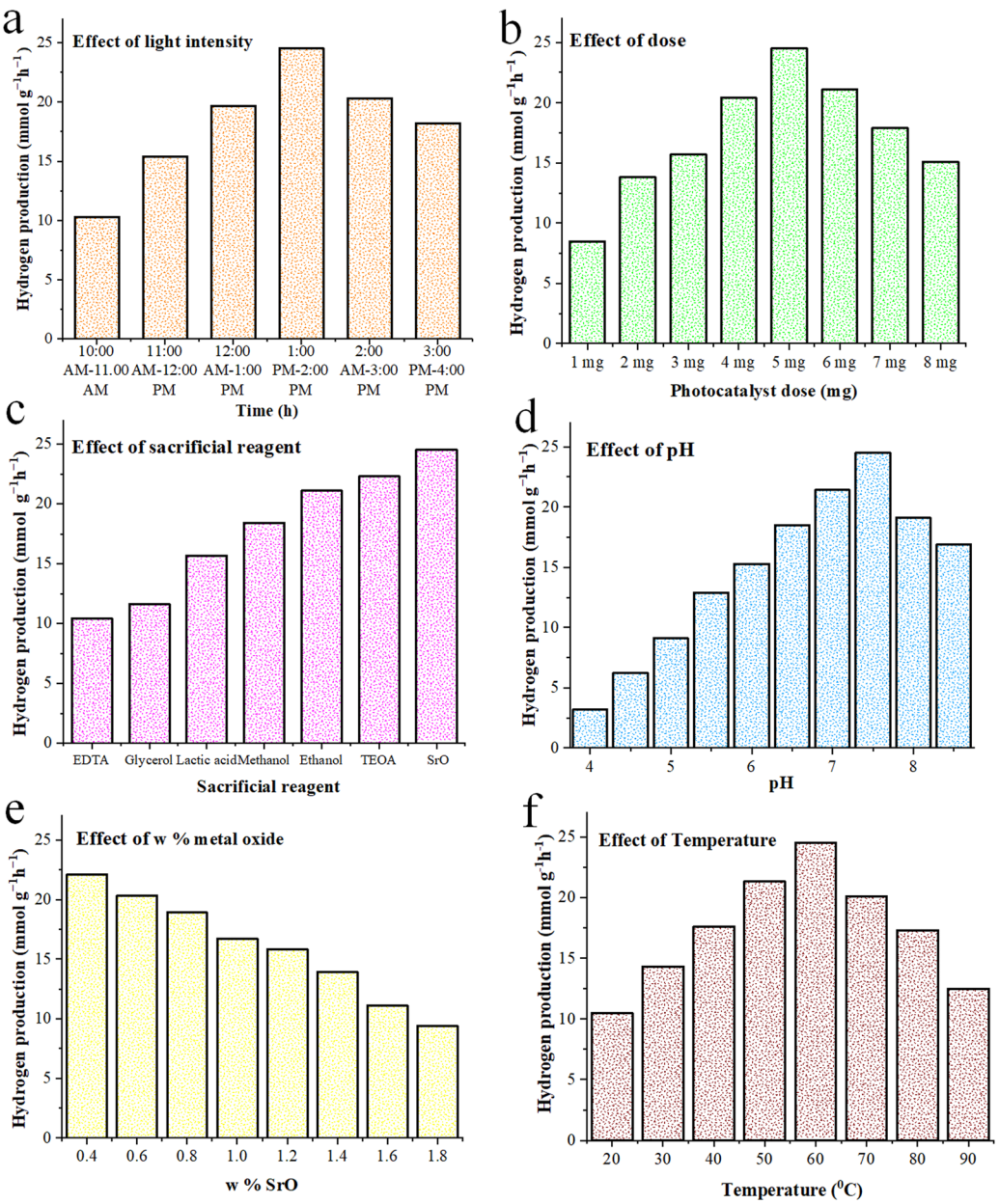

Fig. 7 Representing the factors effecting the rate of hydrogen production (mmol g^{-1} h^{-1}), (a) effect of light intensity, (b) effect of dose, (c) effect of sacrificial reagent, (d) effect of pH, (e) effect of w% metal oxide loading, and (f) effect of temperature.

Recyclability/sustainability test

In current study, the most efficient photocatalyst was found to be Pd–SrO@TiO_2/gCN. The photocatalysts were passed through three runs of recyclability tests. The sustainability of the photocatalysts was demonstrated over a continuous period of 18 hours, as shown in Table S1 (ESI†) and Fig. 5(d). Remarkably, Pd–SrO@TiO_2/gCN did not degrade even after 6 h of reaction and was easily collected for further reactions. To recover the photocatalysts, they were subjected to centrifugation (at 4000 rpm/4–6 minutes), followed by washing and then drying in an oven at 80 °C for 2 hours. Although the process of washing and drying resulted in a slight decrease in the rate of H_2 evolution, it was necessary to ensure their proper preparation for the subsequent run. Fig. S5 (ESI†) compares the XRD patterns of fresh and spent Pd–SrO@TiO_2/gCN catalysts. It is evident from results that the catalyst is stable and can be reused.

Factors effecting the rate of H_2 evolution

The factors, *i.e.*, light intensity, pH, concentration dose, temperature, sacrificial reagents, and wt% loading of SrO over Pd–SrO@TiO_2/gCN and their effects on the rate of hydrogen evolution are illustrated in Tables S2–S7 (ESI†) and Fig. 7(a)–(f) and thoroughly described in Section S2 of the ESI.†

Conclusion

This current research presents a successful development and implementation of a water splitting system for efficient H_2 production without using sacrificial reagents. All photocatalysts were hydrothermally synthesized to achieve the optimal morphology. It was determined that Pd–SrO@TiO_2/gCN exhibited the highest level of photocatalytic activity among all the prepared photocatalysts. The examination of the photocatalysts involved crystallinity and structural evaluation, optical studies and electronic property analyses, morphological analysis, and determination of chemical and elemental compositions *via* XRD, UV-DRS, FTIR, Raman, PL, SEM/EDS, BET, EIS, AFM, EIS and XPS techniques. Analytical investigations of the hydrogen evolution activity performed by each synthesized catalyst in the series were conducted, and subsequently, a thorough comparison was made among them. Remarkably, Pd–SrO@TiO_2/gCN exhibited the impressive hydrogen evolution rate of 24.5 mmol g^{-1} h^{-1} at pH 7.5, surpassing the hydrogen generated by TiO_2, gCN, TiO_2/gCN, SrO@TiO_2/gCN and Pd@TiO_2/gCN. The staggered band alignment between TiO_2/gCN, the Schottky effect exhibited by palladium at the M/S interface, the consumption of holes by SrO as well as enhancement of the Fermi level resulted in boosted charge separation and increased availability of electrons for H^+ ion reduction to H_2. The highest photocatalytic activity of Pd–SrO@TiO_2/gCN is attributed to the palladium in pure metallic state and to SrO. Furthermore, the absence of sacrificial reagents led to the prevention of oxidized product formation, ultimately resulting in maximum evolution of hydrogen. Recyclability tests (3 runs) were employed to assess the sustainability of Pd–SrO@TiO_2/gCN. Numerous factors such as sunlight intensity, sacrificial reagent, wt% loading of SrO, temperature, preparatory techniques and those of the catalysts have been observed to affect the efficiency of the photocatalysts for hydrogen generation *via* water splitting reaction. Improving these factors can enhance the photocatalytic hydrogen generation performance of Pd–SrO@TiO_2/gCN.

Conflicts of interest

The authors declare no competing financial interest.

Acknowledgements

This work was financially supported by the Higher Education Commission (HEC) of Pakistan with grant no. 377/IPFP-II (Batch-I) SRGP/NAHE/HEC/2020/27. Inorganic Material Laboratory (52S), Institute of Chemistry-IUB is credited for the synthesis work and hydrogen production activities. Dr Ejaz Hussain acknowledges Lahore University of Management Sciences (LUMS), University of Karachi (HEJ/ICCBS) and Carnegie Mellon University (CMU)-USA for facilitating the scientific support.

References

1 X. Li, *et al.*, A critical review on integrated system design of solar thermochemical water-splitting cycle for hydrogen production, *Int. J. Hydrogen Energy*, 2022, **47**(79), 33619–33642.
2 N. Abas, *et al.*, Nature inspired artificial photosynthesis technologies for hydrogen production: barriers and challenges, *Int. J. Hydrogen Energy*, 2020, **45**(41), 20787–20799.
3 F. Naaz and T. Ahmad, Ag-Doped WO_3 Nanoplates as Heterogenous Multifunctional Catalyst for Glycerol Acetylation, Electrocatalytic and Enhanced Photocatalytic Hydrogen Production, *Langmuir*, 2023, **39**(27), 9300–9314.
4 V. B.-Y. Oh, S.-F. Ng and W.-J. Ong, Is photocatalytic hydrogen production sustainable?—Assessing the potential environmental enhancement of photocatalytic technology against steam methane reforming and electrocatalysis, *J. Cleaner Prod.*, 2022, **379**, 134673.
5 V. Kyriakou, *et al.*, An electrochemical haber-bosch process, *Joule*, 2020, **4**(1), 142–158.
6 W.-H. Chen, *et al.*, Hydrogen production from partial oxidation and autothermal reforming of methanol from a cold start in sprays, *Fuel*, 2021, **287**, 119638.
7 C. S. Gopinath and N. Nalajala, A scalable and thin film approach for solar hydrogen generation: a review on enhanced photocatalytic water splitting, *J. Mater. Chem. A*, 2021, **9**(3), 1353–1371.
8 M. N. Issac and B. Kandasubramanian, Effect of microplastics in water and aquatic systems, *Environ. Sci. Pollut. Res.*, 2021, **28**, 19544–19562.

9 T. Hisatomi and K. Domen, Reaction systems for solar hydrogen production *via* water splitting with particulate semiconductor photocatalysts, *Nat. Catal.*, 2019, **2**(5), 387–399.
10 S. Bera, *et al.*, Effect of metal doping in Bi_2WO_6 microflowers for enhanced photoelectrochemical water splitting, *Ceram. Int.*, 2022, **48**(23), 35814–35824.
11 M. Jalil, *et al.*, Insight into the development and proceedings of Au@Al–$CeVO_4$ catalysts for water splitting: an advanced outlook for hydrogen generation with sunlight, *Catal. Sci. Technol.*, 2024, **14**(4), 850–862.
12 S. Surendran, *et al.*, Sulphur Assisted Nitrogen-Rich CNF for Improving Electronic Interactions in Co–NiO Heterostructures Toward Accelerated Overall Water Splitting, *Adv. Mater. Technol.*, 2023, **8**(2), 2200572.
13 H. Luo, *et al.*, Topological quantum materials for energy conversion and storage, *Nat. Rev. Phys.*, 2022, **4**(9), 611–624.
14 A. O. M. Almayyali, H. R. Jappor and H. O. Muhsen, High hydrogen production in two-dimensional GaTe/ZnI_2 type-II heterostructure for water splitting, *J. Phys. Chem. Solids*, 2023, **178**, 111317.
15 W. Zhang, *et al.*, Construction of novel PG/GeP_2 and PG/SiP_2 vdW heterostructures for high-efficiency photocatalytic water splitting, *Appl. Surf. Sci.*, 2023, **608**, 155106.
16 R. Sánchez-Tovar, *et al.*, ZnO/ZnS heterostructures for hydrogen production by photoelectrochemical water splitting, *RSC Adv.*, 2016, **6**(36), 30425–30435.
17 M. Z. Abid, *et al.*, Interface engineering of $BiVO_4$/$Zn_3V_2O_8$ heterocatalysts for escalating synergism: Impact of Cu electron mediator for overall water splitting, *Renewable Energy*, 2024, 120223.
18 W. Xu, *et al.*, Overall Water Splitting on The NiS/NiS_2 Heterostructures Featuring Self-Equilibrium Orbital Occupancy, *Adv. Energy Mater.*, 2023, 2300978.
19 J. Zhu, *et al.*, 2D porous Co–Mo nitride heterostructures nanosheets for highly effective electrochemical water splitting, *Appl. Surf. Sci.*, 2023, **623**, 156989.
20 B. Zhang, *et al.*, Construction of a novel Bi-MOF/$BiVO_4$ heterojunction with enhanced visible light photocatalytic performance, *J. Environ. Chem. Eng.*, 2023, 110417.
21 W. He, *et al.*, SnO_2@MoS_2 heterostructures grown on nickel foam as highly efficient bifunctional electrocatalyst for overall water splitting in alkaline media, *J. Alloys Compd.*, 2023, **938**, 168678.
22 M. Jia, *et al.*, Polarization and built-in electric field improve the photocatalytic overall water splitting efficiency of C_2N/ZnSe heterostructures, *Int. J. Hydrogen Energy*, 2023, **48**(51), 19554–19563.
23 Z. Li, *et al.*, MOF-derived ultrasmall Ru@RuO_2 heterostructures as bifunctional and pH-universal electrocatalysts for 0.79 V asymmetric amphoteric overall water splitting, *Chem. Eng. J.*, 2023, **460**, 141672.
24 W. Huang, *et al.*, Molecular heterostructures of covalent triazine frameworks for enhanced photocatalytic hydrogen production, *Angew. Chem., Int. Ed.*, 2019, **131**(26), 8768–8772.
25 Q. Lu, *et al.*, Boosting photocatalytic H_2 production performance over perovskite/CdS quantum dots S-scheme photocatalyst, *J. Alloys Compd.*, 2023, 171074.
26 E. Huusain, Sunlight-Driven Hydrogen Generation: Acceleration of Synergism between Cu–Ag Cocatalysts on a CdS System, *ACS Appl. Energy Mater.*, 2024, **7**(5), 1914–1926.
27 M. Z. Abid, *et al.*, Scope, evaluation and current perspectives of MXene synthesis strategies for state of the art applications, *J. Mater. Chem. A*, 2024, **12**(13), 7351–7395.
28 S. Shanmugaratnam, *et al.*, Recent progress and approaches on transition metal chalcogenides for hydrogen production, *Energies*, 2021, **14**(24), 8265.
29 C. Yavuz and S. E. Ela, Fabrication of g-C_3N_4-reinforced CdS nanosphere-decorated TiO_2 nanotablet composite material for photocatalytic hydrogen production and dye-sensitized solar cell application, *J. Alloys Compd.*, 2023, **936**, 168209.
30 M. I. Taipabu, *et al.*, A critical review of the hydrogen production from biomass-based feedstocks: Challenge, solution, and future prospect, *Process Saf. Environ. Prot.*, 2022, **164**, 384–407.
31 M. Shahrezaei, *et al.*, Ultrasound-Driven Defect Engineering in TiO_{2-x} Nanotubes – Toward Highly Efficient Platinum Single Atom-Enhanced Photocatalytic Water Splitting, *ACS Appl. Mater. Interfaces*, 2023, **15**(31), 37976–37985.
32 G.-C. Yang, *et al.*, Heteropolyacids supported on hierarchically macro/mesoporous TiO_2: efficient catalyst for deep oxidative desulfurization of fuel, *Tungsten*, 2022, 1–10.
33 J. R. Xavier, Influence of surface modified mixed metal oxide nanoparticles on the electrochemical and mechanical properties of polyurethane matrix, *Front. Chem. Sci. Eng.*, 2023, **17**(1), 1–14.
34 T. K. Vo, Bimetallic NiMo-supported Al_2O_3@TiO_2 core-shell microspheres with high hydrodeoxygenation efficiency toward syringol, *J. Sol-Gel Sci. Technol.*, 2023, **105**(3), 804–813.
35 H. Yin, Improved neural network construction of semiconductor TiO_2 magnetic materials by photoacoustic techniques, *Optik*, 2023, **272**, 170272.
36 M.-R. Kim, *et al.*, Photovoltaic Effects of Dye-Sensitized Solar Cells Using Double-Layered TiO_2 Photoelectrodes and Pyrazine-Based Photosensitizers, *ACS Omega*, 2023, **8**(16), 14699–14709.
37 T. Luo, *et al.*, Fabrication of TiO_2/CdS Heterostructure by Soluble Solid-State Titanium-oxo-Clusters for Fast Photocatalytic Degradation of Tetracycline, *J. Phys. Chem. C*, 2023, **127**(3), 1372–1380.
38 K. Rafiq, Tuning of TiO_2/CdS Hybrid Semiconductor with Au Cocatalysts: State-of-the-Art Design for Sunlight-Driven H_2 Generation from Water Splitting, *Energy Fuels*, 2024, **38**(5), 4625–4636.
39 P. Ma, *et al.*, Band alignment of homojunction by anchoring CN quantum dots on g-C_3N_4 (0D/2D) enhance photocatalytic hydrogen peroxide evolution, *Appl. Catal., B*, 2022, **300**, 120736.
40 H. Zhao, *et al.*, High-efficiency hydrogen evolution reaction photocatalyst for water splitting of type-II β-AsP/g-C_3N_4 van

der Waals heterostructure, *Int. J. Hydrogen Energy*, 2023, **48**(27), 10051–10061.

41 H. Y. Hafeez, *et al.*, Insights into hybrid TiO_2-g-C_3N_4 heterostructure composite decorated with rGO sheet: A highly efficient photocatalyst for boosted solar fuel (hydrogen) generation, *Chem. Phys. Impact.*, 2023, **6**, 100157.

42 H. Yu, *et al.*, Alkali-assisted synthesis of nitrogen deficient graphitic carbon nitride with tunable band structures for efficient visible-light-driven hydrogen evolution, *Adv. Mater.*, 2017, **29**(16), 1605148.

43 J.-Y. Tang, *et al.*, Two-dimensional interface engineering of g-C_3N_4/g-C_3N_4 nanohybrid: Synergy between isotype and pn heterojunctions for highly efficient photocatalytic CO_2 reduction, *Chem. Eng. J.*, 2023, **466**, 143287.

44 A. Shi, *et al.*, Metal-Free Carbon Nitride Nanosheet Supported the Pentacoordinated Silicon Intermediates for Photocatalytic Overall Water Splitting. The, *J. Phys. Chem. Lett.*, 2023, **14**(7), 1918–1927.

45 X. Wang, *et al.*, Supramolecular precursor strategy for the synthesis of holey graphitic carbon nitride nanotubes with enhanced photocatalytic hydrogen evolution performance, *Nano Res.*, 2019, **12**, 2385–2389.

46 Y. Niu, *et al.*, The Synergistic Effect in CdS/g-C_3N_4 Nanoheterojunctions Improves Visible Light Photocatalytic Performance for Hydrogen Evolution Reactions, *Molecules*, 2023, **28**(17), 6412.

47 D. Li, *et al.*, A photocatalytic-microbial coupling system for simultaneous removal of harmful algae and enhanced denitrification: Construction, performance and mechanism of action, *J. Hazard. Mater.*, 2023, **459**, 132233.

48 D. O. Adekoya, M. Tahir and N. A. S. Amin, g-C_3N_4/(Cu/TiO_2) nanocomposite for enhanced photoreduction of CO_2 to CH_3OH and HCOOH under UV/visible light, *J. CO2 Util.*, 2017, **18**, 261–274.

49 P. Babu, S. R. Dash and K. Parida, Mechanistic insight the visible light driven hydrogen generation by plasmonic Au–Cu alloy mounted on TiO_2@B-doped g-C_3N_4 heterojunction photocatalyst, *J. Alloys Compd.*, 2022, **909**, 164754.

50 N. Güy, Directional transfer of photocarriers on CdS/g-C_3N_4 heterojunction modified with Pd as a cocatalyst for synergistically enhanced photocatalytic hydrogen production, *Appl. Surf. Sci.*, 2020, **522**, 146442.

51 U. ur Rehman, *et al.*, Effect of Ni and Mn dopant on thermoelectric power generation performance of ZnO nanostructures synthesized *via* hydrothermal method, *Mater. Chem. Phys.*, 2023, **304**, 127907.

52 K. U. Sahar, *et al.*, Sun-light driven hydrogen generation by Pd/Rb_2O cocatalysts: Escalate the utility of rutile TiO_2 for photocatalytic water splitting, *Colloids Surf., A*, 2023, **674**, 131942.

53 A. A. Ibrahim, A. H. Fakeeha and A. S. Al-Fatesh, Enhancing hydrogen production by dry reforming process with strontium promoter, *Int. J. Hydrogen Energy*, 2014, **39**(4), 1680–1687.

54 L. Wang, *et al.*, Fabrication of Ag/SnS_2/g-C_3N_4 *Z*-scheme-type heterojunction photocatalysts with enhanced LED light-driven photoactivity, *Inorg. Chem. Commun.*, 2023, 111144.

55 I. Majeed, *et al.*, Pd–Ag decorated gC_3N_4 as an efficient photocatalyst for hydrogen production from water under direct solar light irradiation, *Catal. Sci. Technol.*, 2018, **8**(4), 1183–1193.

56 Z. Abid, *et al.*, Proceeding of catalytic water splitting on Cu/Ce@g-C_3N_4 photocatalysts: an exceptional approach for sun light driven hydrogen generation, *Nanoscale*, 2024, **16**(14), 7154–7166.

57 M. Z. Abid, *et al.*, Scaling up the charge transfer on Pd@$Ti_3C_2T_x$–TiO_2 catalysts: a sustainable approach for H_2 generation *via* water splitting, *Mater. Adv.*, 2024, **5**(6), 2238–2252.

58 M. Zhang, *et al.*, Room temperature synthesis of reduced TiO_2 and its application as a support for catalytic hydrogenation, *RSC Adv.*, 2017, **7**(8), 4306–4311.

59 A. Speltini, *et al.*, Rationalization of hydrogen production by bulk gC_3N_4: an in-depth correlation between physicochemical parameters and solar light photocatalysis, *RSC Adv.*, 2018, **8**(69), 39421–39431.

60 T. T. Isimjan, *et al.*, Rational design of Pd-TiO_2/g-C_3N_4 heterojunction with enhanced photocatalytic activity through interfacial charge transfer. Clean, *Energy*, 2019, **3**(1), 59–68.

61 M. Z. Abid, *et al.*, Simultaneous elimination of toxic dyes, ciprofloxacin and Cr(VI) contents from polluted water: escalating surface plasmon electrons of Ag cocatalysts on $BiVO_4$ microstructures, *Environ. Sci.: Water Res. Technol.*, 2023, **9**(9), 2238–2252.

62 M. Xue, *et al.*, The direct synthesis of mesoporous structured MnO_2/TiO_2 nanocomposite: a novel visible-light active photocatalyst with large pore size, *Nanotechnology*, 2008, **19**(18), 185604.

63 C. Marchal, *et al.*, Au/TiO_2–gC_3N_4 nanocomposites for enhanced photocatalytic H2 production from water under visible light irradiation with very low quantities of sacrificial agents. Advanced Energy, *Materials*, 2018, **8**(14), 1702142.

64 K. U. Sahar, *et al.*, Surface sensitization of TiO_2 *via* Pd/Rb_2O cocatalysts: Mechanistic insights to the arsenic elimination from ground drinking water, *J. Environ. Chem. Eng.*, 2023, **11**(6), 111202.

65 E. Hussain, *et al.*, Remarkable effect of BaO on photocatalytic H_2 evolution from water splitting *via* TiO_2 (P25) supported palladium nanoparticles, *J. Environ. Chem. Eng.*, 2019, **7**(1), 102729.

66 E. Hussain, *et al.*, Titania-supported palladium/strontium nanoparticles (Pd/Sr-NPs@ P25) for photocatalytic H_2 production from water splitting., *J. Phys. Chem. C*, 2016, **120**(31), 17205–17213.

67 X. Jing, *et al.*, g-C_3N_4 doping TiO_2 recovered from spent catalyst for H_2 evolution from water, *Int. J. Hydrogen Energy*, 2023, **48**(48), 18338–18351.

68 X. Zhang, Layered g-C_3N_4/TiO_2 nanocomposites for efficient photocatalytic water splitting and CO_2 reduction: a review, *Mater. Today Energy*, 2022, **23**, 100904.

69 P. Jiménez-Calvo, *et al.*, Au/TiO_2 (P25)-gC_3N_4 composites with low gC_3N_4 content enhance TiO_2 sensitization for

remarkable H_2 production from water under visible-light irradiation, *Nano Energy*, 2020, **75**, 104888.
70 K. U. Sahar, *et al.*, Surface sensitization of gC_3N_4/TiO_2 *via* Pd/Rb_2O co-catalysts: accelerating water splitting reaction for green fuel production in the absence of organic sacrificial agents, *React. Chem. Eng.*, 2023, **8**(10), 2522–2536.
71 K. Dhumal, R. Dateer and A. Mali, Recent Catalytic Advancements in Organic Transformations Using Biogenically Synthesized Palladium Nanoparticles, *Catal. Lett.*, 2023, 1–23.